

## FINITE ELEMENT ANALYSIS OF ENLARGED END PILES USING FRICTIONAL CONTACT

DAICHAO SHENG<sup>i)</sup>, HARUYUKI YAMAMOTO<sup>ii)</sup> and PETER WRIGGERS<sup>iii)</sup>

### ABSTRACT

This paper presents a modified finite element formulation of frictional contact for soil-pile interaction. This modified formulation is based on smoothed discretisation of the pile surface using BÉZIER polynomials. The finite element code based on this formulation is then used to analyse the loading of piles with enlarged ends of different shapes. Very simple material models are used to represent the behaviour of the soil and the pile. The numerical predictions are compared with the laboratory measurements. It is demonstrated that the new finite element formulation can produce reasonable results for the pile loading problem that involves large interfacial sliding and surface separation.

**Key words:** enlarged end piles, finite element method, frictional contact, smooth discretisation (IGC: E12/E13/K7)

### INTRODUCTION

Numerical modelling of installation and loading of piles and cone penetration tests are generally challenging because the soil-structure interfaces usually involve large deformation, large frictional sliding, large variation of material stiffness and surface separation and reclosure. There has been quite some research on analysing pile driving and pile loading. However, existing methods of simulation either neglect the pile and directly impose a displacement field onto the soil, or use interface elements to represent the soil-pile interaction. In the former case, the true displacement field that the soil experiences is not known and thus has to be assumed. In the latter case, interface elements can only be used for small deformation and can not handle surface separation and re-closure. On the other hand, the approach using contact constraints to represent the soil-structure interaction is not limited to the shortcomings of existing methods. More recent studies on soil-structure interaction using contact constraints have achieved some interesting results (Sheng et al., 2005, 2006). However, contact constraints are very difficult to apply to surface with sharp corners. The sudden change of the surface norm often leads to numerical oscillation and even analysis breakdown (Simo and Meschke, 1993; Sheng et al., 1995).

Non-displacement piles with enlarged ends are often used in foundation engineering to increase the end bearing of the pile capacity. Numerical modelling of these piles is very useful for understanding and estimating the pile bearing capacity, but is further challenged by possible mesh distortion caused by the enlarged pile ends.

This paper presents a finite element formulation of frictional contact for analysing piles with enlarged ends. It first presents a modified formulation based on smooth discretisation of the pile surface. The new formulation is then used to analyse a series of laboratory tests carried out for enlarged end piles with different end shapes and under different overburden pressures.

### SMOOTH DISCRETISATION OF FRICTIONAL CONTACT

The finite element formulation of frictional contact for soil-structural interfaces follows that by Sheng et al. (2006). In this study, one important modification is made to the existing formulation. For penetration problems, using straight segments with sharp corners for the penetrating body tends to cause mesh tangling and oscillation (Sheng et al., 1995). It is thus proposed here to smooth the pile surface. A smooth discretisation based on the BÉZIER polynomials is therefore presented in this paper. To put this smooth discretisation into context, we have to briefly recall the finite element formulation based on the penalty method.

#### *Kinematics at the Interface*

Consider a system of solid bodies in contact. Contact kinematics state that for any admissible displacement, there is no inter-penetration between any two bodies. The normal contact constraints can be represented as

$$g_N \geq 0 \quad (1)$$

where  $g_N$  is the gap between the two bodies. In large

<sup>i)</sup> Professor, School of Engineering, University of Newcastle, NSW 2308, Australia (Daichao.Sheng@newcastle.edu.au).

<sup>ii)</sup> Associate Professor, Graduate School of International Development and Cooperation, Hiroshima University, Japan.

<sup>iii)</sup> Professor, Institut fuer Baumechanik und Numerische Mechanik, University of Hannover, Germany.

The manuscript for this paper was received for review on March 6, 2006; approved on November 22, 2007.

Written discussions on this paper should be submitted before September 1, 2008 to the Japanese Geotechnical Society, 4-38-2, Sengoku, Bunkyo-ku, Tokyo 112-0011, Japan. Upon request the closing date may be extended one month.

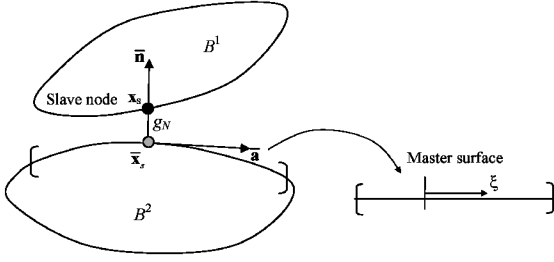


Fig. 1. Definition of closest point projection

deformation mechanics this gap is computed by a closest point projection of a point on the boundary of one body (body 2, called the slave surface  $S$ , Fig. 1), to the surface of the other body (body 1, called the master surface  $M$ ). This leads to the formula

$$g_N = (\mathbf{x}_s - \bar{\mathbf{x}}_s) \cdot \bar{\mathbf{n}} \quad (2)$$

where  $\mathbf{x}_s$  is the current coordinates of the slave node, the bar describes the closest point projection on the master surface, and  $\bar{\mathbf{n}}$  is the normal vector of the master surface at the projection point.

For frictional contact one has to describe the relative tangential motion at the contact interface between the two bodies. This can be performed by defining the relative tangential velocity as

$$\dot{\mathbf{g}}_T = \frac{d}{dt} \{ [1 - \bar{\mathbf{n}} \otimes \bar{\mathbf{n}}] (\mathbf{x}_s - \bar{\mathbf{x}}_s) \} \quad (3)$$

### Penalty Method and Coulomb Friction

Using the penalty method for normal contact yields the relationship

$$t_N = \varepsilon_N g_N \quad (4)$$

where  $t_N$  is the normal component of the traction vector at the contact interface,  $\varepsilon_N$  is a penalty parameter for the normal contact, and  $g_N$  is the gap defined in Eq. (2). In the case of frictionless contact this is the only stress at the contact interface.

In the case of frictional contact, the tangential component of the traction vector at 2D contact interface is

$$t_{Tn} = \begin{cases} \varepsilon_T (g_{Tn} - g_{Tn-1}^{sl}) & \text{for stick, if } \varepsilon_T (g_{Tn} - g_{Tn-1}^{sl}) \leq \mu \cdot t_{Nn} \\ \mu \cdot t_{Nn} & \text{for slip, otherwise} \end{cases} \quad (5)$$

where  $t_{Tn}$  is the tangential component of the traction at time level  $t_n$ ,  $\varepsilon_T$  is a penalty parameter for the tangential contact,  $g_{Tn}$  is the total tangential gap at  $t_n$ ,  $g_{Tn-1}^{sl}$  is the slip part of the tangential gap at  $t_{n-1}$ ,  $t_{Nn}$  is the normal component of the traction at  $t_n$ . Note that Eq. (5) can also be used to detect the modes of the tangential movement.

### Finite Element Formulation of Frictional Contact

The principle of virtual work states that if  $\delta \mathbf{u}$  are virtual displacement fields satisfying the displacement boundary conditions, then equilibrium is satisfied provided

$$\sum_{\alpha} \left( - \int_{V^{\alpha}} \delta \boldsymbol{\varepsilon}^T \boldsymbol{\sigma} dV + \int_{V^{\alpha}} \delta \mathbf{u}^T \mathbf{b} dV + \int_{S_{\sigma}^{\alpha}} \delta \mathbf{u}^T \mathbf{t} dS \right) + \int_{S_c} (t_N \delta g_N + t_T \delta g_T) dS = 0 \quad (6)$$

where  $\delta \boldsymbol{\varepsilon}$  denotes the variation of the strain tensor,  $\boldsymbol{\sigma}$  is the stress tensor,  $\mathbf{b}$  is the body force vector,  $\mathbf{t}$  is the distributed force acting on the boundary  $S_{\sigma}$  of the volume  $V$ ,  $\delta g_N$  and  $\delta g_T$  are the virtual normal and tangential gap, respectively, and the summation is over the number of bodies. When finite deformations are considered, the stress and strain measures in will depend on the configuration (volume and boundaries) used. For an updated Lagrangian formulation as used in this paper, the readers may refer to Nazem et al. (2006) for details.

When the penalty method is used, the normal and tangential tractions can be replaced by the normal and tangential gap functions using Eq. (4) and (5), respectively, which can in turn be expressed as functions of the displacements. To solve the weak form (6), we must first discretise the domain as well as the contact interfaces. In the following, we consider the discretisation of contact interfaces that undergo large sliding motions such as those occurring in the pile penetration process.

### Smooth Discretisation of the Contact Surfaces

One approach that is widely used in nonlinear finite element simulation of contact problems is the so-called node-to-segment contact element as depicted in Fig. 2. Here, contact constraint is enforced for each slave node while the master surface is discretised into straight or curved, smooth segments. The formulation for straight discretisation of master surface can be found in Wriggers (2002) or Sheng et al. (2006). In pile penetration problems, using straight segments for the pile surface tends to cause mesh tangling and it is thus preferable to use smooth segments. We now present a smooth discretisation of the master surface using BÉZIER polynomials.

Assume that the discrete slave node  $\mathbf{x}_s$  comes into contact with the master segment  $\mathbf{x}_1 - \mathbf{x}_2$ , as shown in Fig. 2. We then need the neighbouring nodes  $\mathbf{x}_0$  and  $\mathbf{x}_3$  to define a complete interpolation between  $\mathbf{x}_1$  and  $\mathbf{x}_2$ . For that we use two interpolating polynomials, defined by two mid-nodes (midway between the two master nodes) and two tangent vectors. The mid-nodes  $\mathbf{x}_{01}$  and  $\mathbf{x}_{12}$  represent end-points of the polynomial, while the tangent vectors,  $\mathbf{x}_1 - \mathbf{x}_0$  and  $\mathbf{x}_2 - \mathbf{x}_1$  are defined by a line between the master surface nodes. The geometry so defined is called the 1st interpolation of the active segment defined by nodes  $\mathbf{x}_1$  and  $\mathbf{x}_2$ . The 2nd interpolation is defined by the end points  $\mathbf{x}_{12}$  and  $\mathbf{x}_{23}$  and the tangents  $\mathbf{x}_2 - \mathbf{x}_1$  and  $\mathbf{x}_3 - \mathbf{x}_2$ . The polynomial which has the minimum distance to the slave node  $\mathbf{x}_s$  must be chosen as the active one. The selection is based on the value of the surface coordinate on the segment  $\mathbf{x}_2 - \mathbf{x}_1$ , and this value is computed from

$$\eta = (\mathbf{x}_s - \mathbf{x}_1) \cdot \frac{\mathbf{x}_2 - \mathbf{x}_1}{\|\mathbf{x}_2 - \mathbf{x}_1\|^2} \quad 0 \leq \eta \leq 1 \quad (7)$$

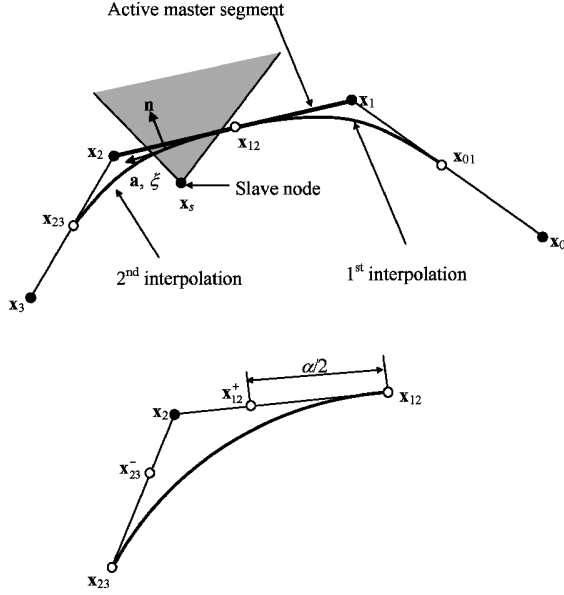


Fig. 2. Node-to-segment contact: smooth discretisation of the master surface,  $\xi \in [-1, +1]$

Since the mid point  $\mathbf{x}_{12}$  is located at  $\eta = \frac{1}{2}$  we can define the 1st interpolation by  $\eta \leq \frac{1}{2}$  and the 2nd interpolation by  $\eta > \frac{1}{2}$ . The relevant interpolation is used to calculate the contact residual and the associated tangent matrix. For simplicity, we suppose that the second polynomial defined by  $\mathbf{x}_{12}$  and  $\mathbf{x}_{23}$  is closer to the slave node, thus all vectors and matrices are described with respect to this interpolation. The interpolation can now be defined as

$$\mathbf{x}(\xi) = B_1(\xi)\mathbf{x}_{12} + B_2(\xi)\mathbf{x}_{12}^+ + B_3(\xi)\mathbf{x}_{23}^- + B_4(\xi)\mathbf{x}_{23} \quad (8)$$

where the standard BÉZIER interpolation functions are given in the APPENDIX.

Observe that the interpolation is with respect to the segment  $\mathbf{x}_{12} - \mathbf{x}_{23}$  in the coordinate  $\xi \in [-1, +1]$ . It lies in the convex hull spanned by the nodes  $\mathbf{x}_{12}$ ,  $\mathbf{x}_{12}^+$ ,  $\mathbf{x}_{23}^-$  and  $\mathbf{x}_{23}$ , where  $\mathbf{x}_{12}^+$  and  $\mathbf{x}_{23}^-$  are on the tangent  $\mathbf{x}_{12} - \mathbf{x}_2$  and  $\mathbf{x}_{23} - \mathbf{x}_2$ , respectively (see Fig. 2), and defined by

$$\mathbf{x}_{12}^+ = \mathbf{x}_{12} + \frac{\alpha}{2}(\mathbf{x}_2 - \mathbf{x}_{12}), \quad \mathbf{x}_{23}^- = \mathbf{x}_{23} + \frac{\alpha}{2}(\mathbf{x}_2 - \mathbf{x}_{23})$$

The parameter  $\alpha$  specifies how far the nodes  $\mathbf{x}_{12}^+$  and  $\mathbf{x}_{23}^-$  are away from the nodes  $\mathbf{x}_{12}$  and  $\mathbf{x}_{23}$ , respectively. For different values of  $\alpha$ , the shape of the surface interpolation changes. In the limit for  $\alpha \rightarrow 0$ , we obtain an almost flat segment. However, the corner region between adjacent segments is still  $C^1$  continuous. Since the shape of the surface changes during the finite deformation process,  $\alpha$  could be adapted as the calculation proceeds. We found in our analysis that a good choice is  $\alpha = 1/6$ .

Since  $\mathbf{x}_{12} = \frac{1}{2}(\mathbf{x}_1 + \mathbf{x}_2)$  and  $\mathbf{x}_{23} = \frac{1}{2}(\mathbf{x}_2 + \mathbf{x}_3)$  we can define in this case the following interpolation and its derivative

$$\mathbf{x}(\xi) = \sum_{i=1}^3 \bar{B}_i(\xi)\mathbf{x}_i, \quad \mathbf{x}_{,\xi}(\xi) = \sum_{i=1}^3 \bar{B}_{i,\xi}(\xi)\mathbf{x}_i. \quad (9)$$

Since the boundary is not straight, it is not possible to obtain a closed form solution for the projection of the

slave node  $\mathbf{x}_s$  onto the master surface. Hence an iterative algorithm has to be used.

For convenience, let a bar on top of a quantity denote that it is evaluated at the projection point  $\bar{\xi}$  or  $\xi_{i+1}$ . Starting from the nonlinear equation which defines the solution point  $\xi$  with minimal distance between the slave node and the master segment

$$[\mathbf{x}_s - \bar{\mathbf{x}}_s(\bar{\xi})] \cdot \bar{\mathbf{n}}_{s,\xi}(\bar{\xi}) = 0 \quad (10)$$

we can devise a Newton algorithm by solving the linearised form

$$\begin{aligned} & \{\bar{\mathbf{x}}_{s,\xi}(\bar{\xi}_i) \cdot \bar{\mathbf{n}}_{s,\xi}(\bar{\xi}_i) - [\mathbf{x}_s - \mathbf{x}_s(\bar{\xi}_i)] \cdot \bar{\mathbf{n}}_{s,\xi\xi}(\bar{\xi}_i)\} \Delta \bar{\xi}_{i+1} \\ & = [\mathbf{x}_s - \mathbf{x}_s(\bar{\xi}_i)] \cdot \bar{\mathbf{n}}_{s,\xi}(\bar{\xi}_i) \\ & \bar{\xi}_{i+1} = \bar{\xi}_i + \Delta \bar{\xi}_{i+1} \end{aligned} \quad (11)$$

This yields  $\bar{\xi}_{i+1}$  as the location of the normal projection of the slave node on to the master surface. It will also be denoted by  $\bar{\xi}$  in the following.

A good choice for a starting value of this iteration is provided by the projection onto the straight line defined by  $\mathbf{x}_2$  and  $\mathbf{x}_1$ . Noting  $-1 \leq \xi \leq +1$ , we then have

$$\xi_0 = 2 \frac{(\mathbf{x}_s - \mathbf{x}_1) \cdot (\mathbf{x}_2 - \mathbf{x}_1)}{(\mathbf{x}_2 - \mathbf{x}_1) \cdot (\mathbf{x}_2 - \mathbf{x}_1)} - 1 \quad (12)$$

The expression for the gap and its variation are now

$$\begin{aligned} g_{Ns} &= \left[ \mathbf{x}_s - \sum_{i=1}^3 \bar{B}_i(\bar{\xi})\mathbf{x}_i \right] \cdot \bar{\mathbf{n}}, \\ \delta g_{Ns} &= \left[ \delta \mathbf{u}_s - \sum_{i=1}^3 \bar{B}_{i,\xi}(\bar{\xi})\delta \mathbf{u}_i \right] \cdot \bar{\mathbf{n}} \end{aligned} \quad (13)$$

where  $\delta \mathbf{u}$  is the variation of displacements. The variation is easily expressed in matrix form as

$$\delta g_{Ns} = \delta \bar{\mathbf{u}}_s^T \mathbf{B}_N(\bar{\xi}) = \langle \delta \mathbf{u}_s^T, \delta \mathbf{u}_1^T, \delta \mathbf{u}_2^T, \delta \mathbf{u}_3^T \rangle \begin{Bmatrix} \bar{\mathbf{n}} \\ -\bar{B}_1(\bar{\xi})\bar{\mathbf{n}} \\ -\bar{B}_2(\bar{\xi})\bar{\mathbf{n}} \\ -\bar{B}_3(\bar{\xi})\bar{\mathbf{n}} \end{Bmatrix} \quad (14)$$

Using the finite element formulation of the gap variation, the residual connected with the smooth BÉZIER approximation can be stated. For the penalty method, the weak form of the normal contact

$$\int_{S_c} t_N \delta g_N dS = \int_{S_c} \varepsilon_N g_N \delta g_N dS$$

is approximated by

$$\begin{aligned} C_c &= \int_{S_c} t_N \delta g_N dS = \int_{S_c} \varepsilon_N g_N \delta g_N dS \\ &\approx \sum_{s=1}^{n_c} \delta \bar{\mathbf{u}}_s^T [\varepsilon_N A_s g_{Ns} \mathbf{B}_N(\bar{\xi})]. \end{aligned} \quad (15)$$

This leads to the vector form of the contact residual for one slave node  $s$  and the associated segment

$$\mathbf{F}_{Ns}^c = \varepsilon_N A_s g_{Ns} \mathbf{B}_N(\bar{\xi}). \quad (16)$$

The linearisation of (15) is given by

$$\Delta C_N \approx \sum_{s=1}^{n_s} \varepsilon_N A_s (\delta g_{N_s} \Delta g_{N_s} + g_{N_s} \Delta g_{N_s}) = \sum_{s=1}^{n_s} \delta \tilde{\mathbf{u}}_s^T (\mathbf{K}_{N_s} \Delta \tilde{\mathbf{u}}_s) \quad (17)$$

where the tangent matrix for one slave node  $s$  is given

$$\begin{aligned} \mathbf{K}_{N_s} = & \varepsilon_N A_s \{ \mathbf{B}_N(\bar{\xi})(\mathbf{B}_N(\bar{\xi}))^T - g_{N_s} [\mathbf{B}_{N_s, \xi}(\bar{\xi})(\mathbf{B}_{\xi}(\bar{\xi}))^T \\ & + \mathbf{B}_{\xi}(\bar{\xi})(\mathbf{B}_{N_s, \xi}(\bar{\xi}))^T + \bar{b}_{\xi\xi} \mathbf{B}_{\xi}(\bar{\xi})(\mathbf{B}_{\xi}(\bar{\xi}))^T \\ & - \frac{g_{N_s}}{\|\bar{\mathbf{x}}_{s, \xi}\|^2} [\mathbf{B}_{N_s, \xi}(\bar{\xi}) + \bar{b}_{\xi\xi} \mathbf{B}_{\xi}(\bar{\xi})] [\mathbf{B}_{N_s, \xi}(\bar{\xi}) \\ & + \bar{b}_{\xi\xi} \mathbf{B}_{\xi}(\bar{\xi})]^T] \} \end{aligned} \quad (18)$$

which is based on the smooth BÉZIER formulation for normal contact. The undefined quantities in Eq. (18) are given in the APPENDIX.

Note that, for small deformations, one can neglect all terms in (18) which are multiplied by the gap  $g_N$ . This yields a simple expression for the tangent matrix of frictionless smooth contact related to the slave node  $s$  and the associated segment, according to

$$\mathbf{K}_{N_s}^{\text{lin}} = \varepsilon_N A_s \mathbf{B}_N(\bar{\xi}) \mathbf{B}_N(\bar{\xi})^T \quad (19)$$

In case of frictional contact we have to distinguish between stick and slip. This can be done by the evaluation of the slip condition (5). Here we restrict ourselves to the classical Coulomb law. Over a time increment  $\Delta t = t_{n+1} - t_n$ , the incremental tangential displacement is given by  $\dot{g}_T \Delta t = \Delta g_T$ . The vector of the incremental tangential displacement follows Eq. (3) and is given by the change of the surface coordinate  $\xi$  in the time step as

$$\Delta \mathbf{g}_{T_{n+1}} = (\xi_{n+1} - \xi_n) \frac{\partial \bar{\mathbf{x}}_s}{\partial \xi} = (\xi_{n+1} - \xi_n) \bar{\mathbf{x}}_{s, \xi}(\xi_{n+1}) \quad (20)$$

Using this relation the trial stress follows from Eq. (5)

$$\mathbf{t}_{T_{n+1}}^{\text{tr}} = \mathbf{t}_{T_n} + \varepsilon_T \Delta \mathbf{g}_{T_{n+1}} \quad (21)$$

Using now the slip criterion for Coulomb's law

$$f_{n+1} = \|\mathbf{t}_{T_{n+1}}^{\text{tr}}\| + \mu \varepsilon_N g_{N_{n+1}} \leq 0 \quad (22)$$

we can distinguish between slip and stick. For  $f_{n+1} < 0$  we have stick. In that case, the tangential force at the contact point is given by

$$\mathbf{t}_{T_{n+1}} = \mathbf{t}_{T_{n+1}}^{\text{tr}} \quad (23)$$

In the case of slip ( $f_{n+1} \geq 0$ ) and for the Coulomb law, the tangential force is given by

$$\mathbf{t}_{T_{n+1}} = \mu \varepsilon_N g_{N_{n+1}} \mathbf{n}_{T_{n+1}}^{\text{tr}}$$

with

$$\mathbf{n}_{T_{n+1}}^{\text{tr}} = \text{sign}(\xi_{n+1} - \xi_n) \bar{\mathbf{a}}(\xi_{n+1}) \quad (24)$$

In the case of tangential contact, the weak form

$$\int_{S_c} \mathbf{t}_T \cdot \delta \mathbf{g}_T dS$$

is approximated by the sum

$$C_T = \int_{S_c} \mathbf{t}_T \cdot \delta \mathbf{g}_T dS \approx \sum_{s=1}^{n_s} \delta \mathbf{g}_{T_s} \cdot \mathbf{t}_{T_{n+1}} A_s \quad (25)$$

Since  $\mathbf{t}_{T_{n+1}}$  is given for the stick case by (21) and for the

slip case by (24), we only have to compute the variation of the relative tangential displacement. This variation follows Eq. (20) and can be computed by

$$\begin{aligned} \delta \mathbf{g}_{T_s} = & \delta \xi \bar{\mathbf{x}}_{s, \xi}(\xi) = \delta \tilde{\mathbf{u}}_s^T \{ H_{\xi\xi}^{-1} [\mathbf{B}_T(\bar{\xi}) + g_{N_s} \mathbf{B}_{N_s, \xi}(\bar{\xi})] \} \bar{\mathbf{x}}_{s, \xi}(\xi) \\ = & \delta \tilde{\mathbf{u}}_s^T \mathbf{B}_{\xi}(\bar{\xi}) \bar{\mathbf{x}}_{s, \xi}(\xi) \end{aligned} \quad (26)$$

An explicit expression for the residual can then be obtained. Noting that the tangential force can be written as  $\mathbf{t}_{T_{n+1}} = \gamma_{n+1} \bar{\mathbf{a}}(\xi_{n+1})$  where

$$\text{stick: } \gamma_{n+1} = \varepsilon_T (\xi_{n+1} - \xi_n) \|\bar{\mathbf{x}}_{s, \xi}(\xi_{n+1})\| \quad (27)$$

$$\text{slip: } \gamma_{n+1} = -\mu \varepsilon_N g_{N_{n+1}} \text{sign}(\xi_{n+1} - \xi_n) \quad (28)$$

$$\bar{\mathbf{a}}(\xi_{n+1}) = \frac{\bar{\mathbf{x}}_{s, \xi}(\xi_{n+1})}{\|\bar{\mathbf{x}}_{s, \xi}(\xi_{n+1})\|}$$

The residual can be written as

$$\begin{aligned} C_T \approx & \sum_{s=1}^{n_s} \delta \xi \bar{\mathbf{x}}_{s, \xi}(\xi_{n+1}) \cdot \gamma_{n+1} \bar{\mathbf{a}}(\xi_{n+1}) A_s \\ = & \delta \tilde{\mathbf{u}}_s^T \mathbf{B}_{\xi}(\bar{\xi}) \|\bar{\mathbf{x}}_{s, \xi}(\xi_{n+1})\| \gamma_{n+1} A_s \end{aligned} \quad (29)$$

We can derive the matrix form from the previous equation for one slave node  $s$

$$\mathbf{F}_{T_s}^c = \|\bar{\mathbf{x}}_{s, \xi}(\xi_{n+1})\| \gamma_{n+1} A_s \mathbf{B}_{\xi}(\bar{\xi}_{n+1}) \quad (30)$$

In the case of small penetrations, the term  $g_N$  in Eq. (A6) for  $\mathbf{B}_{\xi}(\bar{\xi}_{n+1})$  can be neglected and the formulation (30) simplifies to

$$\mathbf{F}_{T_s}^{\text{clin}} = \gamma_{n+1} A_s \mathbf{B}_T(\xi_{n+1}) \quad (31)$$

where  $\mathbf{B}_T$  is given in the APPENDIX. The linearisation of the residual in (29) leads to the tangent matrix for the linear case. We now have to distinguish between the stick case, which yields the symmetric matrix

$$\mathbf{K}_{T_s}^{\text{st}} = \varepsilon_T A_s \bar{\mathbf{B}}_T(\xi_{n+1}) (\mathbf{B}_T(\xi_{n+1}))^T \quad (32)$$

and the slip case which furnishes

$$\mathbf{K}_{T_s}^{\text{sl}} = -\mu \varepsilon_N \text{sign}(\xi_{n+1} - \xi_n) A_s \bar{\mathbf{B}}_T(\xi_{n+1}) (\mathbf{B}_N(\xi_{n+1}))^T. \quad (33)$$

### Global Equations

Combining Eqs. (6), (15) and (25) leads to the global set of equations

$$\begin{aligned} \sum_{\alpha} \left( - \int_{V^{\alpha}} \delta \boldsymbol{\varepsilon}^T \boldsymbol{\sigma} dV + \int_{V^{\alpha}} \delta \mathbf{u}^T \mathbf{b} dV + \int_{S_g^{\alpha}} \delta \mathbf{u}^T \mathbf{t} dS \right) \\ + \int_{S_c} (t_N \delta g_N + t_T \delta g_T) dS \\ = \delta \mathbf{U}^T (\mathbf{G}(\mathbf{U}) + \mathbf{F}_N^c(\mathbf{U}) + \mathbf{F}_T^c(\mathbf{U})) \\ = \delta \mathbf{U}^T (\mathbf{G}(\mathbf{U}) + \mathbf{G}^c(\mathbf{U})) = \delta \mathbf{U}^T \mathbf{R}(\mathbf{U}) = 0 \end{aligned} \quad (34)$$

where  $\mathbf{U}$  is used in place of  $\mathbf{u}$  to indicate the discretised global displacement field,  $\mathbf{G}(\mathbf{U})$  denotes the domain contributions to the residual vector,  $\mathbf{G}^c(\mathbf{U})$  denotes the contact contributions given by (16) and (30), and  $\mathbf{R}(\mathbf{U})$  is the global residual vector.

The global tangent matrix is obtained by linearising

(34) at a given  $\mathbf{U}$  according to

$$\begin{aligned} \mathbf{K}(\mathbf{U}) &= \frac{\partial \mathbf{R}(\mathbf{U})}{\partial \mathbf{U}} = \frac{\partial (\mathbf{G}(\mathbf{U}) + \mathbf{G}^c(\mathbf{U}))}{\partial \mathbf{U}} \\ &= (\mathbf{K}_{ep}(\mathbf{U}) + \mathbf{K}_{Ns}(\mathbf{U}) + \mathbf{K}_{Ts}(\mathbf{U})) \end{aligned} \quad (35)$$

where  $\mathbf{K}_{ep}$  is the tangent stiffness matrix due to the elastoplastic domains, and  $\mathbf{K}_{Ns}$  and  $\mathbf{K}_{Ts}$  are the tangent matrices due to the normal and tangential contact which are given by Eqs. (18), (32) and (33).

The nonlinear systems of equations defined by (35) can then be solved by the Newton-Raphson scheme presented in Sheng et al. (2006).

### SIMULATION OF PILE TESTS IN SANDY SOILS

A series of laboratory tests have been carried out, to study the effects of end shape and overburden pressure on the bearing capacity of piles with enlarged ends and to study the sand particle movement around the pile tip (Yamamoto et al., 2000). The results from these tests can conveniently be used to validate the numerical method presented above.

In the laboratory tests carried out by Yamamoto et al., steel piles with enlarged ends are buried in a sandy soil contained in a large tank whose diameter is about 10~15 times the pile diameter. These piles were wrapped with thin Teflon sheets along their shafts, to reduce the shaft friction. Such a steel pile was first hung at the centre of the tank. The tank was then filled by Toyoura sand using a sand-spreader assembly method which ensures the sand

is uniformly filled to a relative density of about 90%. Such an experimental setup approximates the installing of non-displacement piles. In addition, a set of surcharge pressures were applied to the sand surface, to simulate stress conditions at different ground depths. To reduce the boundary friction and hence to transfer the applied surcharge pressures uniformly to all depths in the sand, two thin Teflon sheets were adhered to the inner wall of the steel tank with silicon-grease layers. Load cells placed at different depths confirmed the uniform distribution of stresses in the sand. Finally, the pile was pushed steadily down in the sand to a certain displacements, to simulate the loading of the pile.

The boundary conditions and the finite element meshes used for these tests are shown in Fig. 3. Four-noded elements with 4 integration points are used. The pile with a cone angle of  $180^\circ$  or a flat end is approximated by a cone angle of  $170^\circ$ , to facilitate the numerical simulation. The geometry of the enlarged pile head is shown in Fig. 4. To simulate the experimental setup of the tests, the pile is initially in contact with the weightless soil. A pressure load is then applied to the soil top surface, while the pile is allowed to settle vertically with the soil. This step is used to establish an initial stress field in the soil that is in equilibrium with the boundary conditions. Once the initial stresses are set up, all displacements in the soil and the pile are set to zero. The pile is then pushed down in the soil by prescribing a vertical displacement of 50 mm at the pile top. The load-displacement curves of the pile are obtained from this loading step.

The behaviour of the Toyoura sand is represented by a

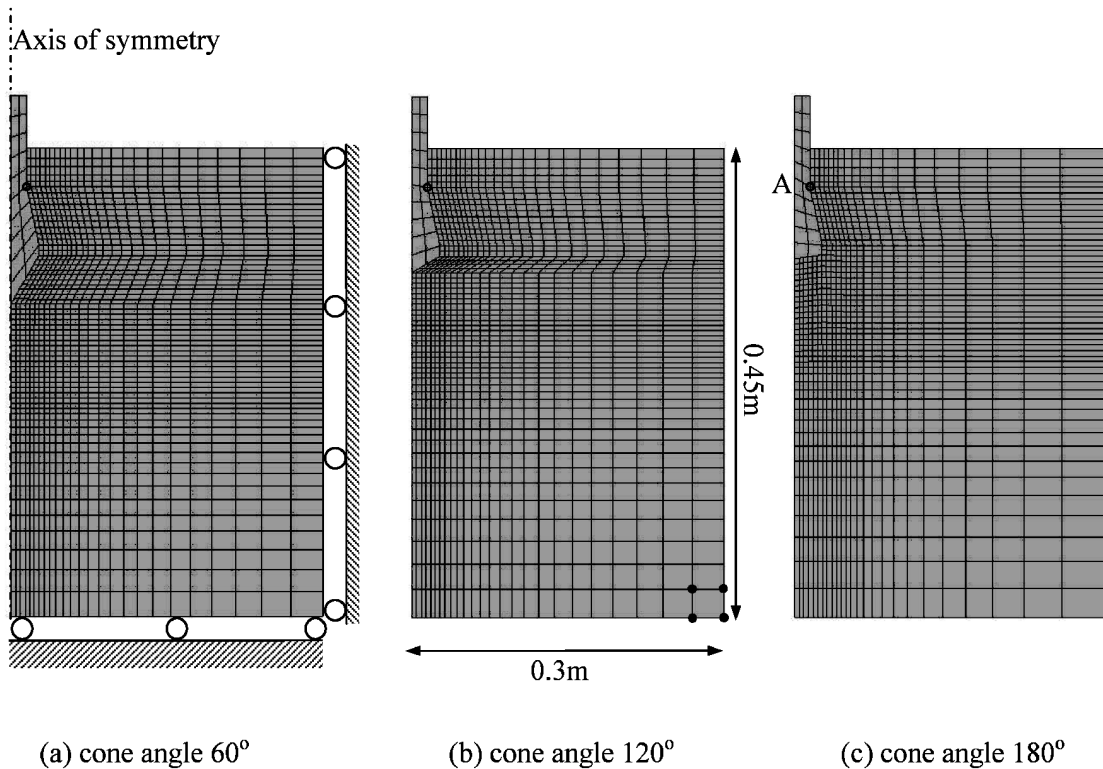


Fig. 3. Finite element meshes (a typical element is shown at the lower right corner)

rounded Mohr-Coulomb model. The yield function or the plastic potential of the model is given as

$$f = \left( \frac{4\beta^4}{1 + \beta^4 - (1 - \beta^4) \sin 3\theta} \right)^{1/4} q - \frac{6 \sin \phi'}{3 - \sin \phi'} p' - \frac{6 \cos \phi'}{3 - \sin \phi'} c' \quad (36)$$

where  $q$  is the deviator stress,  $p'$  is the effective mean stress,  $\phi'$  is the friction angle for the yield function or the dilation angle for the plastic potential,  $c'$  is the cohesion,  $\theta$  is the Lode angle and the parameter  $\beta$  is given by

$$\beta = \frac{3 - \sin \phi'}{3 + \sin \phi'}$$

The yield surface in the deviatoric plane is shown in Fig. 5. This surface is a smoothed convex for  $\phi' \leq 48.6^\circ$  (Sheng et al., 2000). The reason for using the rounded Mohr-Coulomb model instead of the classic Mohr-Coulomb model is to reduce the numerical instability caused by vertices of the yield surfaces of the latter. As shown in Fig. 5, the two models coincide with each other at triaxial compression and extension stress states ( $\theta = \mp 30^\circ$ ). A more advanced model could of course be used to represent the soil behaviour, with the cost of more material parameters. The simple rounded Mohr-Coulomb model has only two strength parameters (friction angle  $\phi'$  and dilation angle  $\psi'$ ) with  $c' = 0$  for the dry sand, in addition to two deformation parameters (Young's modulus  $E$  and Poisson's ratio  $\nu$ ).

According to the data by Yamamoto et al. (2000) and

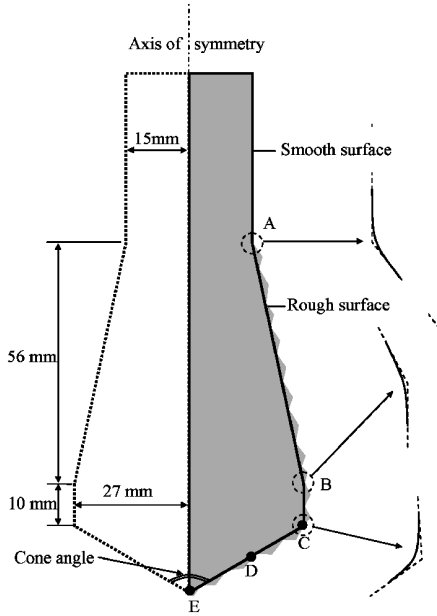


Fig. 4. Pile head configuration with smoothed corners

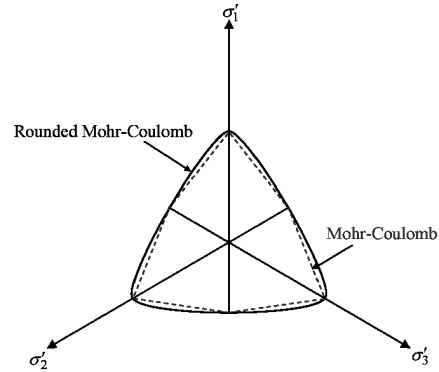


Fig. 5. Yield function in the deviatoric plane for the smoothed Mohr-Coulomb model

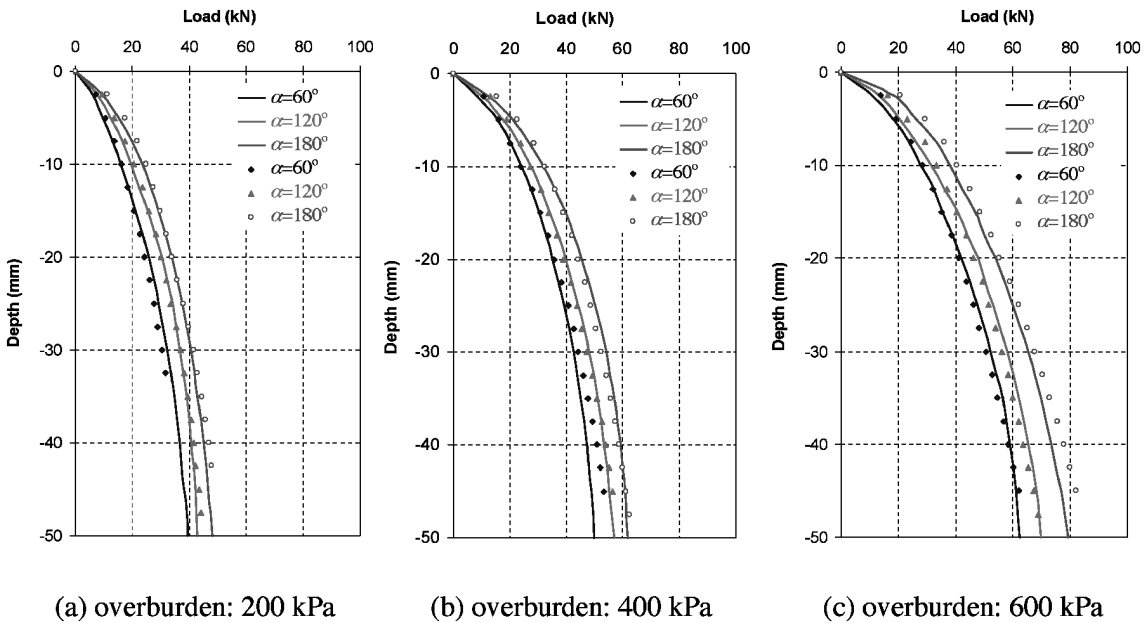


Fig. 6. Comparison of predicted and measured load-displacement curves (solid lines: predicted; dots: measured)

Li and Yamamoto (2005), the friction angle (at critical state) of the sand is  $30^\circ$ , with a dilation angle of  $15^\circ$ . The Poisson ratio of the soil is assumed to be 0.333, which corresponds to a  $K_0$  value of 0.5. The Young modulus of the soil that best fits one of the experimental load-displacement curves is about 98 MPa (*see* discussion about Fig. 6) and therefore a rounded-up value of 100 MPa is used in all the analysis.

The steel pile is assumed to be elastic with a Young's modulus of 200 GPa and Poisson's ratio of 0.3. The pile surface is smoothed according to Fig. 4, with the smoothing parameter  $\alpha$  setting to 1/6. The soil-pile interface is assumed to be smooth along the pile shaft (above point A in Fig. 4), but rough along the pile end (below point A in Fig. 4) with a soil-pile interfacial frictional angle of  $30^\circ$ .

In the simulation, the penalty parameters for normal

and tangential contact are both set to  $10^9$  kN/m<sup>3</sup>, i.e. about 200 times of the soil stiffness divided by the thickness of the soil elements close to the pile. Test runs indicate that this value can be reduced or increased by one order of magnitude, without causing much change of the numerical results. The prescribed displacement at the pile head, i.e. 50 mm penetration, is applied in 1000 equal increments. The Newton-Raphson scheme (Sheng et al., 2006) is used to solve the global equations within each increment. All the analyses are carried out using the finite element code SNAC, developed at the University of Newcastle over the last 10 years or so.

## NUMERICAL RESULTS AND DISCUSSION

In the tests carried out by Yamamoto et al. (2000), a

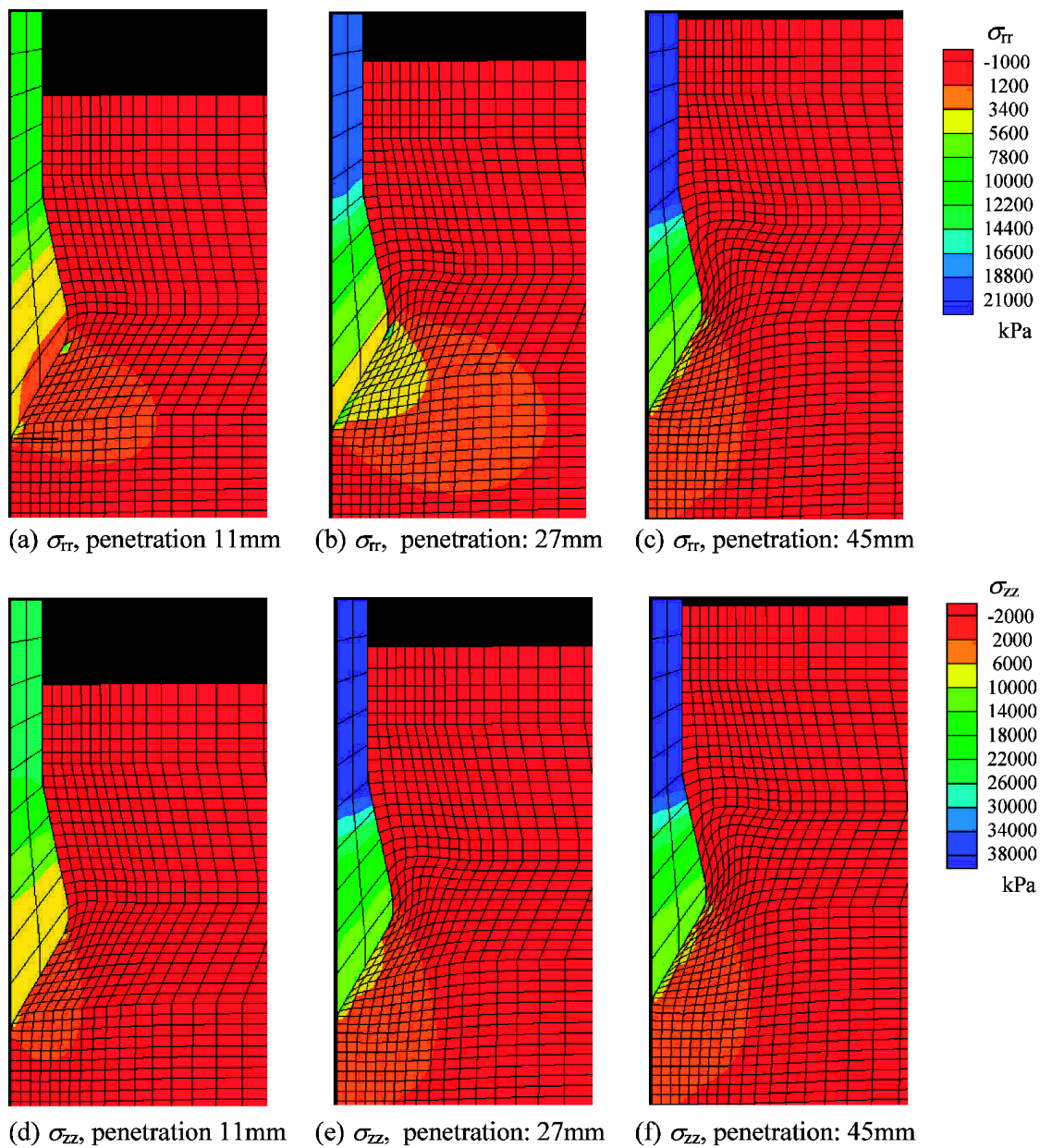
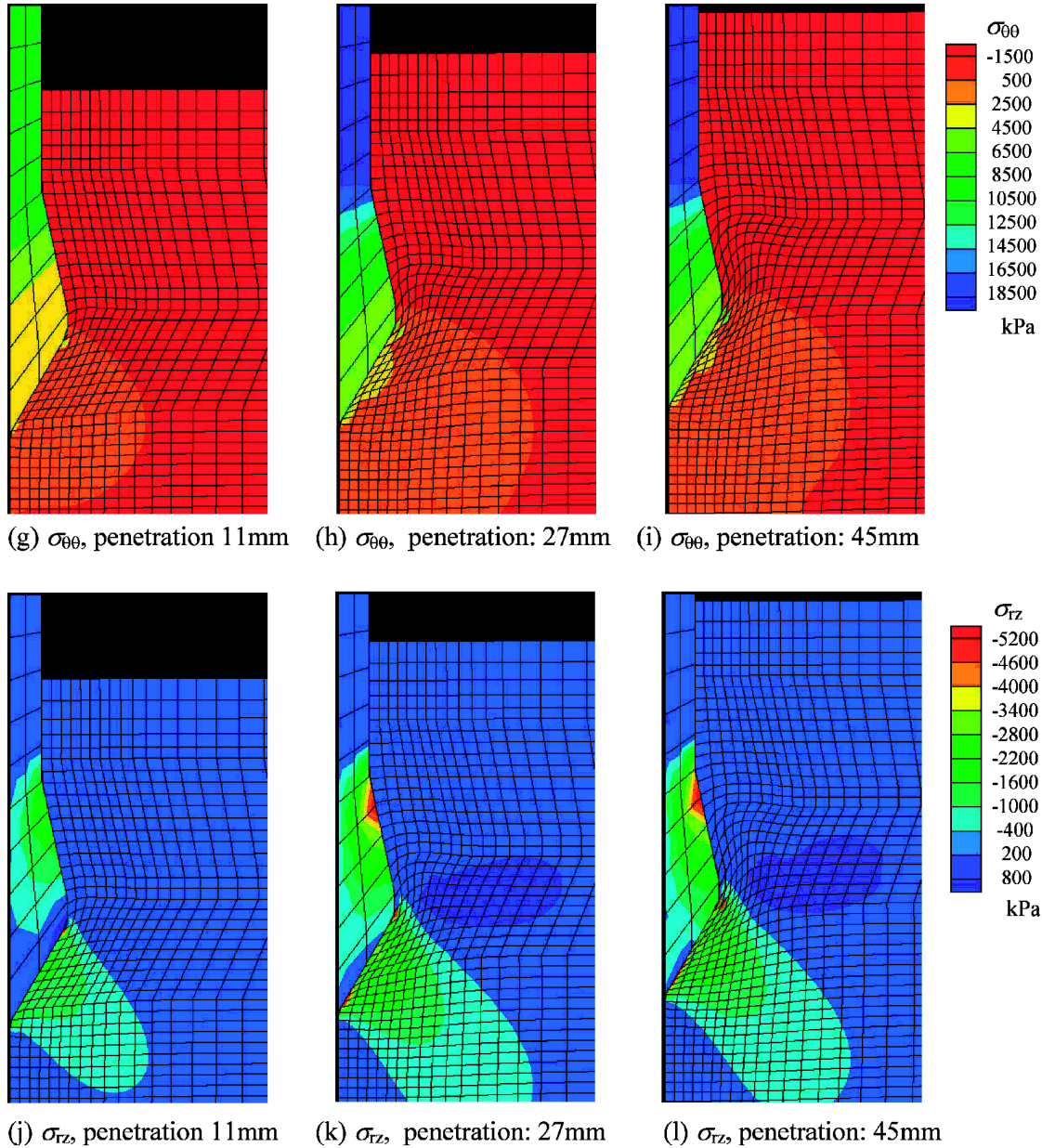


Fig. 7. Deformed mesh and stress contours ( $\sigma_{rr}$ : radial stress;  $\sigma_{zz}$ : vertical stress;  $\sigma_{rz}$ : shear stress;  $\sigma_{\theta\theta}$ : circumferential stress; cone angle  $60^\circ$ ; overburden = 200 kPa)



**Fig. 7. Cont. Deformed mesh and stress contours ( $\sigma_r$ : radial stress;  $\sigma_{rz}$ : vertical stress;  $\sigma_{rz}$ : shear stress;  $\sigma_{\theta\theta}$ : circumferential stress; cone angle  $60^\circ$ ; overburden = 200 kPa)**

load transducer was placed in the pile head, with the pile shaft wrapped with thin layers of Teflon sheets. The loads measured at the transducer are then plotted against the settlement of the pile. In the numerical simulation, the pile is pushed into the soil by prescribed displacements at the pile head. The vertical reaction forces at the pile head are the summed up to the pile load. The pile loads so computed are plotted against the pile penetration in Fig. 6, where the measured pile loads are also shown. As mentioned above, one soil parameter, Young's modulus  $E$ , was best fitted to match the experimental load-displacement for the pile with a cone angle of  $120^\circ$  and an overburden pressure of 400 kPa. The best-fitted value ( $E = 97$  MPa) was then rounded up to 100 MPa and used in all the other analyses. In general, the computed load-displacement curves are very close to the experimental

curves. The maximum discrepancy between the computed and measured loads is about 6.4% which occurs for the case of the pile with a cone angle of  $180^\circ$  and the soil with an overburden of 600 kPa. A noticeable difference between the computed and measured load-displacement curves is that the former seems to be less affected by the cone angle. The curves for the pile with a cone angle of  $120^\circ$  were best predicted by the numerical model (Fig. 6(a)–(c)). The predicted loads for the pile with a cone angle of  $60^\circ$  are generally larger than the corresponding measured values (Fig. 6(a), 6(c)), whereas the loads for the pile with a cone angle of  $180^\circ$  are smaller than the measured values (Fig. 6(a), 6(c)).

Figure 7 shows the deformed meshes and stress contours for the pile with a cone angle of  $60^\circ$  and the overburden pressure of 200 kPa. For each stress component,

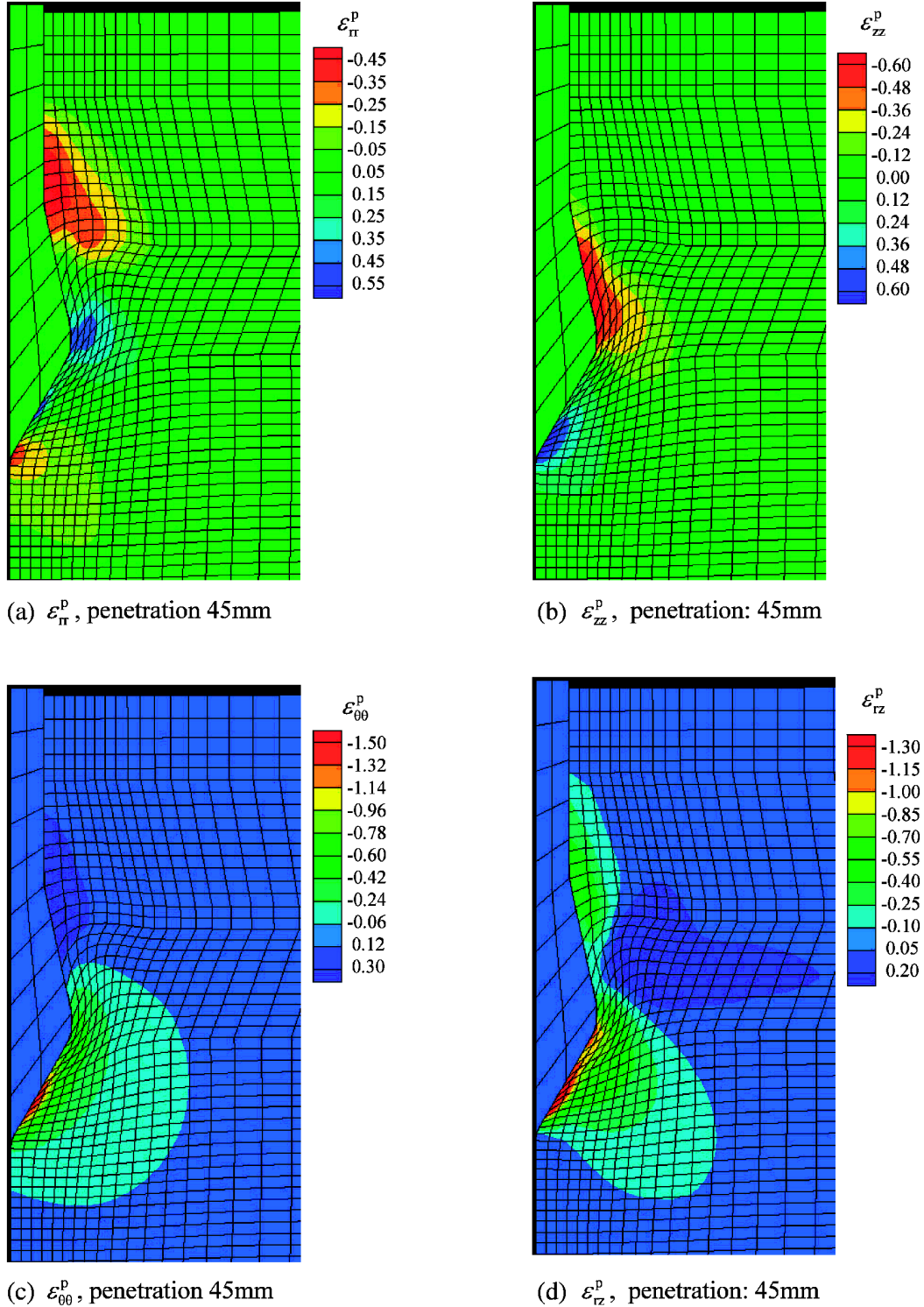


**Fig. 8.** Plastic strain contours ( $\varepsilon_{\pi}^p$ : plastic radial strain;  $\varepsilon_{zz}^p$ : plastic vertical strain;  $\varepsilon_{\theta\theta}^p$ : plastic circumferential strain;  $\varepsilon_{\pi z}^p$ : shear strain; cone angle 120°; overburden = 200 kPa)

the contours are plotted at three specific penetration depths. We first notice that the pile was successfully pushed into soil and large relative sliding occurs along the pile-soil interface, particularly along the pile shaft where the interface is frictionless. Along the upper part of the pile end (part AB in Fig. 4), the soil seems to move downwards together with the pile and no large cavity is left behind the pile. This pattern of deformation is caused by

the friction of the interface and the vertical compressive pressure applied at the soil surface. Along the pile surface BCDE, some relative sliding between the soil and the pile occurs, which has caused some slight distortion of a few soil elements just below the pile end (Fig. 7(c)). In general, the deformed meshes show a reasonable deformation pattern of the soil as the pile is pushed in.

The contours of radial stress ( $\sigma_{\pi}$ ) in Fig. 7(a)–(c) show

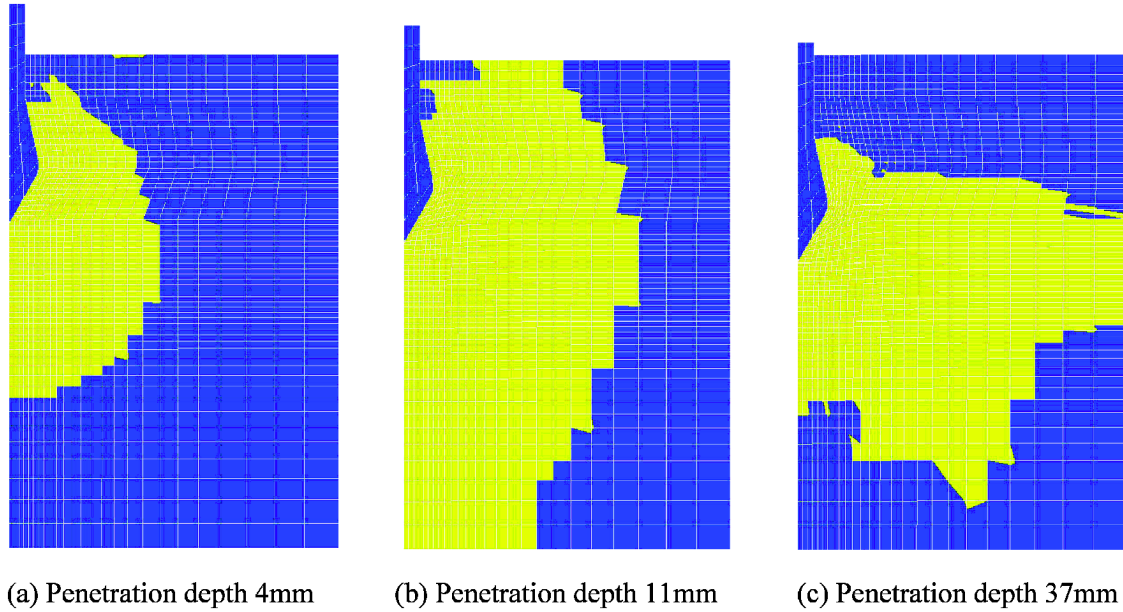


Fig. 9. Active plastic zones (cone angle  $120^\circ$ ; overburden = 200 kPa)

that this stress has increased from an initial homogeneous value of  $-100$  kPa to somewhere between  $4000$ – $10000$  kPa in the elements just beneath the pile end. The compressive stress is taken as positive in all the stress contours. The stress bulb under the pile end increases as the pile penetrates, as expected. In the pile, the highest radial stress occurs at the pile shaft and is around  $20000$  kPa. The lowest  $\sigma_{rr}$  in the pile occurs at the pile conical tip and is around  $7500$  kPa. No tensile radial stresses are observed in the pile.

The contours of the vertical stress ( $\sigma_{zz}$ ) are shown in Fig. 7(d)–(f). The maximum compressive stresses in the soil occur in the elements just below the pile end. At the penetration depth of  $45$  mm, the maximum vertical stress in the soil is around  $-10000$  kPa. The vertical stresses in the pile vary between  $10000$ – $40000$  kPa, with the highest vertical stress in the pile shaft (around  $40000$  kPa) and the lowest in the pile end (around  $10000$  kPa).

The circumferential (hoop) stress ( $\sigma_{\theta\theta}$ ) distributions in the soil and the pile show similar patterns as the radial stress distributions. This stress varies between  $3500$ – $7000$  in the soil elements just beneath the pile end (Fig. 7(g)–(i)), less significant compared to  $\sigma_{rr}$  and  $\sigma_{zz}$ . In the pile, the maximum circumferential stress is around  $18000$  kPa in the pile shaft and the minimum  $5000$  kPa in the pile end. The maximum shear stress ( $\sigma_{rz}$ ) in the soil is around  $4000$  kPa, in the soil elements beneath the pile end (Fig. 7(j)–(l)). The maximum shear stress in the pile is around  $5000$  kPa, near point A where the pile surface changes from smooth to frictional.

The contours of plastic strains at the penetration depth of  $45$  mm are shown in Fig. 8. Again, compressive strains are taken as positive. The plastic radial strain in the soil near the pile changes from tension near the pile tip (point E), to compression near points D, C and B, and to a tension again near point A. The plastic vertical strain in the

soil changes from compression beneath the pile tip to tension along the side CBA. The hoop strain is in tension in the soil beneath the pile end, but in compression around point A. The active plastic zones are shown in Fig. 9. The active plastic zone initially expands until it reaches the top and bottom boundaries (Fig. 9(a)–(b)), and is then deactivated from above and below due to the boundary constraints (Fig. 9(c)).

The stress and strain contours for the pile with a cone angle of  $120^\circ$  are plotted over the deformed meshes at penetration depth of  $21$  mm in Fig. 10. We see that the soil elements beneath the pile end and around the pile shoulder are more distorted than the case for the pile with a cone angle of  $60^\circ$ . Again, large relative sliding occurs along the pile shaft and along the surface BA. However, very little relative sliding occurs along the pile end (the segment CDE in Fig. 4). The maximum radial, vertical and circumferential stresses in the soil again occur in the elements just beneath the pile conical end. The maximum radial, vertical and circumferential stresses in the pile again occur in the pile shaft. The radial stress in the pile tip (point E) smaller than those at points D and C. The plastic radial strain  $\epsilon_{rr}^p$  in the soil changes from tension beneath the pile end (near point D), to compression near point B and then to tension near point A. The plastic vertical strain  $\epsilon_{zz}^p$  changes from compression beneath the pile end EDC) to tension above the pile shoulder (CBA). The plastic circumferential strain changes from tension below EDC to compression along BA.

For the pile with a cone angle of  $180^\circ$ , the deformed meshes shown in Fig. 11 are also distorted, particularly for the elements near the corner of the pile ends. This mesh distortion is due to the Updated Lagrangian method used in the analysis. It may even cause some small negative radial displacements at the axis of symmetry. To overcome such mesh distortion, more advanced

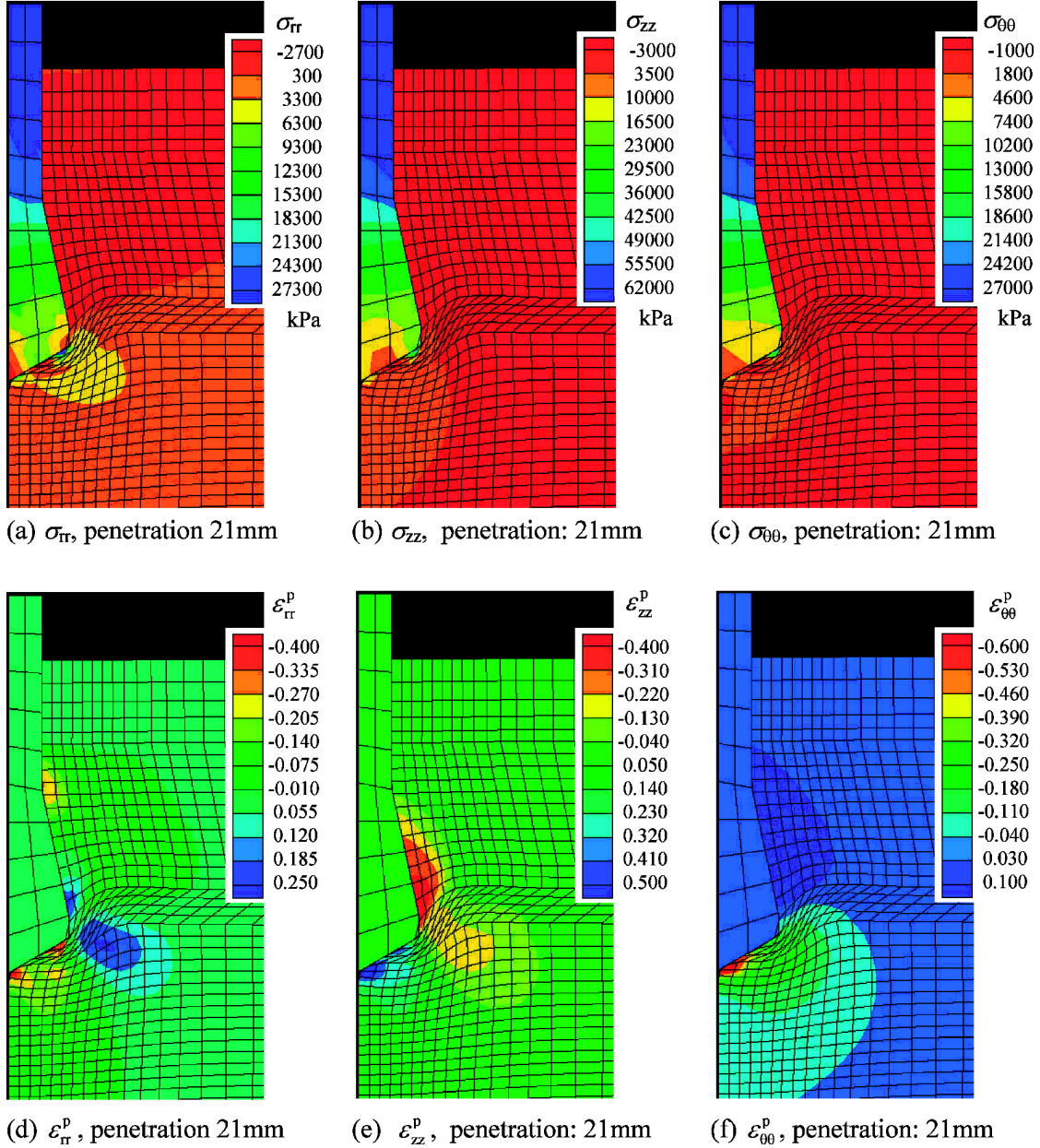


**Fig. 10.** Deformed mesh and stress and strain contours ( $\sigma_{rr}$ : radial stress;  $\sigma_{zz}$ : vertical stress;  $\sigma_{\theta\theta}$ : circumferential stress; radial plastic strain;  $\varepsilon_{zz}^p$ : vertical plastic strain;  $\varepsilon_{\theta\theta}^p$ : circumferential strain; cone angle  $120^\circ$ ; overburden = 200 kPa)

methods, such as the Arbitrary Lagrangian-Eulerian method (Nazem et al., 2006), may have to be used. Figures 11 also show some element overlapping near the corner of the pile end (position C in Fig. 4). This overlapping is partly due to the relatively coarse linear elements used, and partly due to the smoothing of the pile surface around the corner. In theory the mesh should be kept as fine as possible, particularly around the pile where strain is large. However, a very fine mesh may not be able to produce a numerical solution, due to possibly severe mesh distortion.

The maximum values of  $\sigma_{rr}$ ,  $\sigma_{zz}$  and  $\sigma_{\theta\theta}$  in the soil in Fig. 11 are higher than those observed for the piles with a cone angle of  $60^\circ$  or  $120^\circ$ . The stress distributions in the soil are of similar patterns as those with a cone angle of

$60^\circ$  and  $120^\circ$ . As for the pile with a conical end of  $120^\circ$ , the radial stress in the pile centre (point E) is lower than those near the edge of the end (point C), indicating the potential of tensile cracking at the centre. Indeed, the radial stress at point E can evolve to a negative value. This tensile radial stress is not shown in Fig. 11(a) due to the low resolution of the stress contours. The results confirm the experimental observation that a concrete or cement pile with a flat end may develop tensile cracks at its centre, which is the exact reason that a conical end is usually used instead. The plastic strain contours in Fig. 11(d)–(f) show similar patterns as those in Fig. 8 and Fig. 10.

Figure 12 shows the deformed mesh and the zoom-up of pile-soil surface for the pile with a cone angle of  $60^\circ$ .

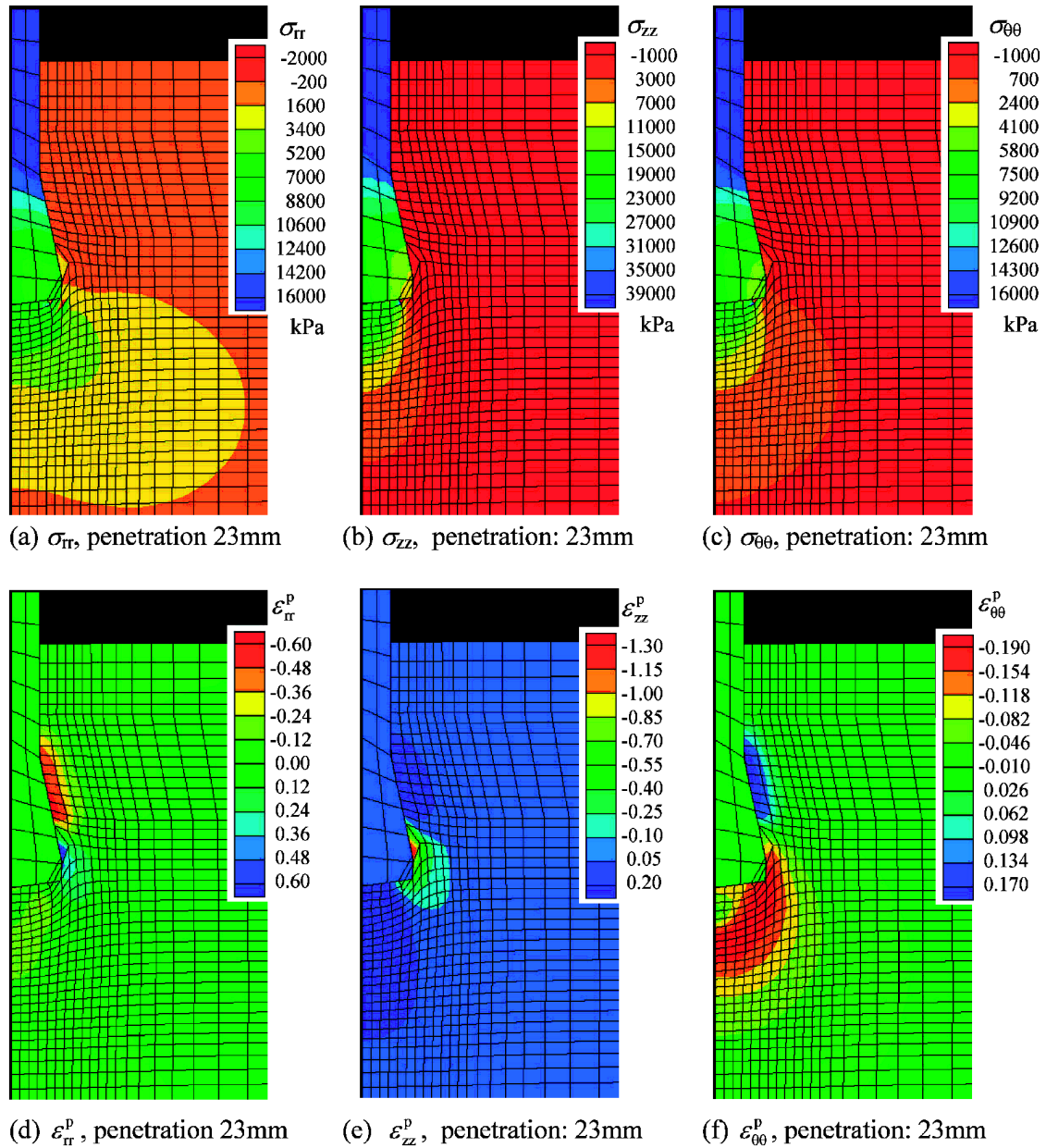


**Fig. 11.** Deformed mesh and stress contours ( $\sigma_{rr}$ : radial stress;  $\sigma_{zz}$ : vertical stress;  $\sigma_{rz}$ : shear stress;  $\sigma_{\theta\theta}$ : circumferential stress; cone angle  $180^\circ$ ; overburden = 200 kPa)

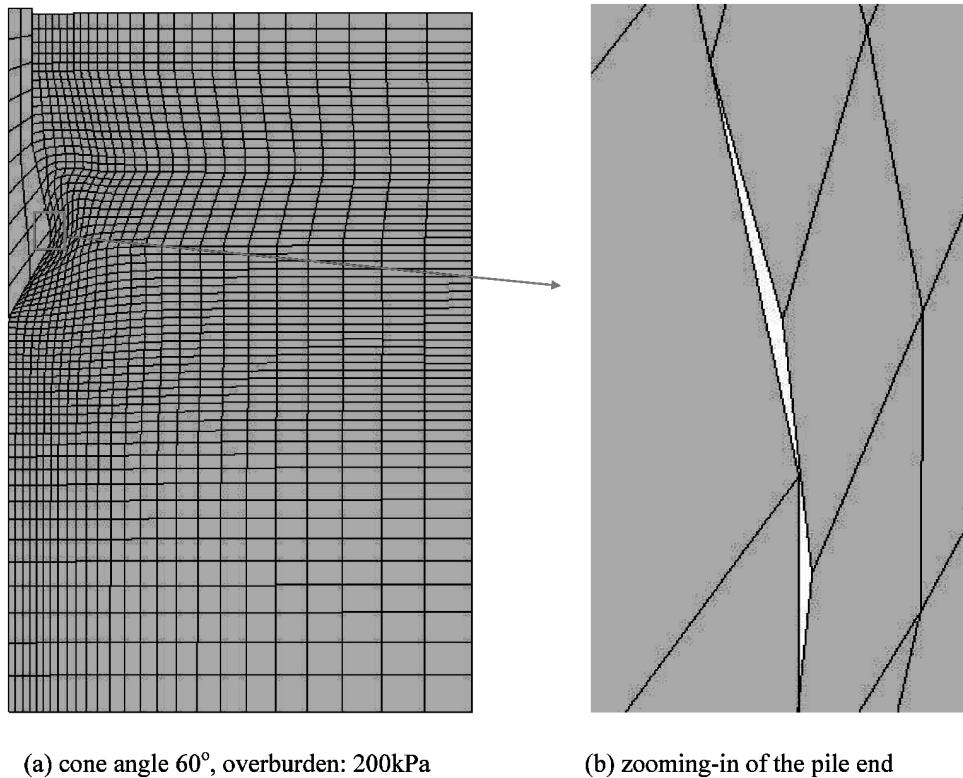
In this figure, large relative sliding along the pile-soil interface can be noticed. The magnified part of the mesh clearly shows the surface separation and re-closure between the soil and the pile (Fig. 12(b)). Such an interfacial behaviour can not be modelled with interface or joint elements.

Another note that should be made here is the possible particle crushing caused by the high stresses generated beneath the pile end. The maximum mean stresses in the soil are in the order of 10000 kPa, which is sufficient to cause particle crushing of the sand. To take into account the crushing phenomenon, we will have to use more advanced soil models that will eventually need more material parameters. Such elaboration should in theory lead to more reliable results if the material parameters could be estimated with confidence. On the other hand, we have in

this paper used a simple soil model and back-estimated one key material parameter and have achieved satisfactory results. The back-estimated parameter (in this case the Young modulus of the soil) may not represent the true value of the soil, but reflects the combined effects of the other facts such as particle crushing. Such a simplified approach can of course be very useful if we can carry out the back-estimation with confidence.

## CONCLUSIONS

This paper presents a modified formulation of friction contact for the soil-pile interaction. The modified formulation is based on the smooth discretisation of the pile surface using the BÉZIER polynomials. The finite element model based on this new formulation is then used to ana-



(a) cone angle 60°, overburden: 200kPa

(b) zooming-in of the pile end

Fig. 12. Zoom-up of the deformed mesh, showing pile-soil separation (penetration depth: 45 mm)

lyse pile loading tests in Toyoura sand. The steel piles have enlarged ends with different shapes and are modelled as an elastic material. The Toyoura sand is modelled by a rounded Mohr-Coulomb model. It is demonstrated that, even with the simplified approach to model the soil and pile behaviour, the new finite element formulation is able to produce reasonable results for the pile loading problem. Such a problem involves large interfacial sliding and surface separation and would be very difficult to solve otherwise.

The numerical analysis presented in this paper can be improved in a number of aspects. For example, more advanced numerical algorithms can be used to tackle the mesh distortion problem associated with large deformation. The constitutive model used for the soil is too simplistic and more advanced models, particularly those with the capability to model particle crushing, can be incorporated into the analysis. In addition, the soil analysed in this study is assumed to be completely dry. In the future, coupled analysis that takes into account both deformation and pore pressure generation/dissipation can be developed and applied. Formulation incorporating impact elements can also be developed to tackle dynamic loading of piles.

#### ACKNOWLEDGEMENT

The research carried out in this paper is sponsored by the Australian Research Council (ARC) Discovery Project (DP0557161), which also includes a visiting grant to support the visit of the second author (H. Yamamoto)

to the University of Newcastle during October and November of 2005. This financial support from ARC is appreciated.

#### REFERENCES

- 1) Li, W., Ikeda, K., Yamamoto, H. and Tominga, K. (2003): Measurement of soil displacement around pile tip by digital image analysis, *Geotechnical Engineering in Urban Construction* (eds. by Yu, Y. and Akagi, H.), Tsinghua University Press, Beijing, China, 393-400.
- 2) Li, W. and Yamamoto, H. (2005): Numerical analysis on soil behaviour around pile-tip under vertical load, *Journal of Structural and Construction Engineering (Transaction of AIJ)*, **51B**, 147-157.
- 3) Nazem, M., Sheng, D. and Carter, J. P. (2006): Stress integration and meshing refinement for large deformation in geomechanics, *International Journal for Numerical Methods in Engineering*, **65**, 1002-1027.
- 4) Sheng, D., Axelsson, K. and Magnusson, O. (1997): Stress and strain fields around a penetrating cone, *Numerical Models in Geomechanics* (eds. by Pietruszczak, S. and Pande, G. N.), Balkema, Rotterdam, 653-660.
- 5) Sheng, D., Sloan, S. W. and Yu, H. S. (2000): Aspects of finite element implementation of critical state models, *Computational Mechanics*, **26**, 185-196.
- 6) Sheng, D. and Sloan, S. W. (2001): Load stepping methods for critical state models, *International Journal for Numerical Methods in Engineering*, **50**, 67-93.
- 7) Sheng, D., Eigenbrod, K. D. and Wriggers, P. (2005): Finite element analysis of pile installation using large-slip frictional contact, *Computers and Geotechnics*, **32**(1), 17-26.
- 8) Sheng, D., Sun, D. A. and Matsuoka (2006): Cantilever sheet-pile wall modelled by frictional contact, *Soils and Foundations*, **46**(1), 29-37.
- 9) Simo, J. C. and Meschke, G. (1993): A new class of algorithms for

classical plasticity extended to finite strains. Application to geomaterials, *Computational Mechanics*, **11**(4), 253–278.

- 10) Wriggers, P. (2002): *Computational Contact Mechanics*, John Wiley & Sons, Chichester.
- 11) Yamamoto, H., Xu, T. and Tominaga, K. (2000): Effects of overburdening pressures and end shapes on bearing capacities of underreamed end piles, *Developments in Geotechnical Engineering* (eds. by Balasubramaniam, A. S. et al.), Asian Institute of Technology, Bangkok, Thailand, 255–261.

## APPENDIX: BÉZIER INTERPOLATION FUNCTIONS

The standard BÉZIER polynomials are given as follows

$$\begin{aligned}
 B_1(\xi) &= \frac{1}{8} (1 - \xi)^3 \\
 B_2(\xi) &= \frac{3}{8} (1 - \xi)^2 (1 + \xi) \\
 B_3(\xi) &= \frac{3}{8} (1 - \xi) (1 + \xi)^2 \\
 B_4(\xi) &= \frac{1}{8} (1 + \xi)^3
 \end{aligned} \tag{A1}$$

When we use the special interpolation defined in Fig. 1, the BÉZIER interpolation is based on three nodes with the interpolation functions

$$\begin{aligned}
 \bar{B}_1(\xi) &= \frac{1}{2} [B_1(\xi) + (1 - \alpha)B_2(\xi)] \\
 \bar{B}_2(\xi) &= \frac{1}{2} [B_1(\xi) + (1 + \alpha)(B_2(\xi) + B_3(\xi)) + B_4(\xi)] \\
 \bar{B}_3(\xi) &= \frac{1}{2} [B_4(\xi) + (1 - \alpha)B_3(\xi)]
 \end{aligned} \tag{A2}$$

Further functions used in the stiffness matrices:

$$\mathbf{B}_N(\bar{\xi}) = \begin{Bmatrix} \bar{\mathbf{n}} \\ -\bar{B}_1(\bar{\xi})\bar{\mathbf{n}} \\ -\bar{B}_2(\bar{\xi})\bar{\mathbf{n}} \\ -\bar{B}_3(\bar{\xi})\bar{\mathbf{n}} \end{Bmatrix} \tag{A3}$$

$$\mathbf{B}_{N,\xi}(\bar{\xi}) = \begin{Bmatrix} 0 \\ \bar{B}_{1,\xi}(\bar{\xi})\bar{\mathbf{n}} \\ \bar{B}_{2,\xi}(\bar{\xi})\bar{\mathbf{n}} \\ \bar{B}_{3,\xi}(\bar{\xi})\bar{\mathbf{n}} \end{Bmatrix} \tag{A4}$$

$$\mathbf{B}_T(\bar{\xi}) = \begin{Bmatrix} \bar{\mathbf{x}}_{s,\xi} \\ -\bar{B}_1(\bar{\xi})\bar{\mathbf{x}}_{s,\xi} \\ -\bar{B}_2(\bar{\xi})\bar{\mathbf{x}}_{s,\xi} \\ -\bar{B}_3(\bar{\xi})\bar{\mathbf{x}}_{s,\xi} \end{Bmatrix} \tag{A5}$$

$$\mathbf{B}_\xi(\bar{\xi}) = H_{\xi\xi}^{-1}[\mathbf{B}_T(\bar{\xi}) + g_N \mathbf{B}_{N,\xi}(\bar{\xi})] \tag{A6}$$

$$H_{\xi\xi}^{-1} = (\bar{a}_{11} - g_N \bar{\mathbf{n}}^1 \cdot \bar{\mathbf{x}}_{,\xi\xi}^1)^{-1} \tag{A7}$$

$$\bar{a}_{11} = \bar{\mathbf{x}}_{,\xi}^1(\bar{\xi}) \cdot \bar{\mathbf{x}}_{,\xi}^1(\bar{\xi}) \tag{A8}$$

$$\bar{b}_{\xi\xi}^1 = \bar{\mathbf{x}}_{,\xi\xi}^1 \cdot \bar{\mathbf{n}}^1 \tag{A9}$$